Simultaneous fMRI and fast-scan cyclic voltammetry bridges evoked oxygen and neurotransmitter dynamics across spatiotemporal scales

Lindsay R Walton[a,b,c,*], **Matthew Verber**[a,b,d], **Sung-Ho Lee**[a,b,c], **Tzu-Hao Harry Chao**[a,b,c], **R. Mark Wightman**[d], **Yen-Yu Ian Shih**[a,b,c,*]

[a] Center for Animal MRI, University of North Carolina at Chapel Hill, Chapel Hill, NC, United States of America

[b] Biomedical Research Imaging Center, University of North Carolina at Chapel Hill, Chapel Hill, NC, United States of America

[c] Department of Neurology, University of North Carolina at Chapel Hill, Chapel Hill, NC, United States of America

[d] Department of Chemistry, University of North Carolina at Chapel Hill, Chapel Hill, NC, United States of America

Abstract

The vascular contributions of neurotransmitters to the hemodynamic response are gaining more attention in neuroimaging studies, as many neurotransmitters are vasomodulatory. To date, well-established electrochemical techniques that detect neurotransmission in high magnetic field environments are limited. Here, we propose an experimental setting enabling simultaneous fast-scan cyclic voltammetry (FSCV) and blood oxygenation level-dependent functional magnetic imaging (BOLD fMRI) to measure both local tissue oxygen and dopamine responses, and global BOLD changes, respectively. By using MR-compatible materials and the proposed data acquisition schemes, FSCV detected physiological analyte concentrations with high temporal resolution and spatial specificity inside of a 9.4 T MRI bore. We found that tissue oxygen

[*] Corresponding authors. waltonlr@email.unc.edu (L.R. Walton), shihy@neurology.unc.edu (Y.-Y.I. Shih).

and BOLD correlate strongly, and brain regions that encode dopamine amplitude differences can be identified via modeling simultaneously acquired dopamine FSCV and BOLD fMRI time-courses. This technique provides complementary neurochemical and hemodynamic information and expands the scope of studying the influence of local neurotransmitter release over the entire brain.

Keywords

Neurovascular coupling; BOLD fMRI; Voltammetry; Dopamine; Hemodynamic response function

1. Introduction

Coupling between neuronal activity and cerebral hemodynamic changes ensures that healthy energetic homeostasis is maintained within the active brain (Iadecola, 2017; Buxton, 2013). Classic blood oxygenation-level dependent functional magnetic resonance imaging (BOLD fMRI) data interpretation assumes that hemodynamic responses to stimuli are proportional to neuronal activity, such that hemodynamic response function (HRF; Iadecola (2017)) can be derived to translate neuronal activity into BOLD signal predictions (Logothetis et al., 2001). However, these assumptions are not always valid. Neurotransmitters have been receiving more attention as contributors to the hemodynamic response, as many are vasomodulatory (e.g., dopamine, nitric oxide, norepinephrine) (Iadecola, 2017; Krimer et al., 1998) and dysregulated in pathologies where neurovascular coupling is also dysregulated, such as schizophrenia and Parkinson's (Iadecola, 2017; Meyer-Lindenberg et al., 2002). It is paramount to understand how specific neurotransmitters influence vascular responses and accurately interpret neuroimaging data throughout the brain.

Dopamine is a vasomodulatory neurotransmitter concentrated in the striatum (Krimer et al., 1998; Choi et al., 2006), and plays a strong role in motivation, movement, addiction, learning, and reward prediction (Brocka et al., 2018). Dopamine receptors most densely populate dendrites and dendritic spines (Yung et al., 1995), but they also exist on microvasculature within the striatum, thalamus, and cortex, as well as on astrocytes (Choi et al., 2006; Miyazaki et al., 2004). Though dopamine has been studied intensely for decades, few studies have delved into its vascular modulation properties. Amphetamine and phencyclidine challenges show a linear relationship between evoked striatal hemodynamic changes and dopamine (Ren et al., 2009; Mandeville et al., 2013; Paasonen et al., 2017), and D1- and D2-like dopamine receptor agonists show diametrically opposed vascular responses (Choi et al., 2006). Though fMRI responses to cocaine and amphetamine challenge have been identified (Mandeville et al., 2013), existing HRF models do not consider dopaminergic influence from shorter release events where higher affinity, presynaptic receptor binding would have more of an impact (Ren et al., 2009). Dissecting how dopamine influences striatal vasculature is an important first step into understanding how whole-brain hemodynamics are affected by dopaminergic neurotransmission.

Popular methods of monitoring dopamine or other neurotransmitter kinetics in vivo are electrochemical, such as fast-scan cyclic voltammetry (FSCV) and amperometry (Bucher

and Wightman, 2015), though advances are being made with fluorescent sensor and magnetic resonance-based detection (Li and Jasanoff, 2020; Patriarchi et al., 2018; Beyene et al., 2019; Sun et al., 2018), among others (Ganesana et al., 2017). FSCV is especially desirable because it is chemically selective and quantifiable, and multiple different neurotransmitters can be detected using well-established modifications (Bucher and Wightman, 2015; Ganesana et al., 2017). It has high spatial specificity, temporal resolution, and minimal tissue damage, especially versus competing techniques like positron emission tomography and microdialysis (Ganesana et al., 2017). FSCV has also been used in humans to study neurotransmission during human behavior (Kishida et al., 2011; Lohrenz et al., 2016; Chang et al., 2012), a challenge for fluorescent sensor-based techniques. Though FSCV can detect both tonic (Oh et al., 2018) and phasic (Belle et al., 2013; Robinson et al., 2003; Park et al., 2010; Garris et al., 1993) dopamine changes, and oxygen changes (Venton et al., 2003; Walton et al., 2017; Zimmerman and Wightman, 1991; Zimmerman et al., 1992), carbon-fiber microelectrodes probe discrete microenvironments within the brain (Walton et al., 2017) that may not reflect larger-scale neurochemical or vascular changes (Thompson et al., 2003). To reveal the influence of local dopamine release on whole brain circuits requires pairing FSCV with fMRI to acquire neurotransmitter and brain-wide hemodynamic data simultaneously.

In this work, we develop and characterize a simultaneous FSCV-fMRI technique. We address the challenges of developing an MR-compatible FSCV recording system, circumventing high-frequency electronic noise from MR imaging gradients, and synchronizing multimodal data acquisition. We perform in vivo FSCV-fMRI during an oxygen inhalation challenge using an oxygen-sensitive FSCV waveform and electrical deep brain stimulation using both oxygen- and dopamine-sensitive FSCV waveforms at an electrode implanted into the nucleus accumbens (NAc). To compare hemodynamic measurements at different spatial scales, we collected tissue oxygen and BOLD fMRI data concurrently. We derive an HRF from high-resolution dopamine data acquired during simultaneous fMRI, and for the first time, we demonstrate that this simultaneous FSCV-fMRI recording platform can identify brain regions that encode dopamine amplitude changes. This method should contribute significantly to the understanding of local neurotransmission on dynamic changes of brain activity.

2. Materials and methods

2.1. Fast scan cyclic voltammetry (FSCV)

Carbon-fiber microelectrodes were fabricated as previously described (Clark et al., 2010), with modifications for MRI compatibility. Briefly, a 5–7 μm-diameter carbon fiber (Thornel T-650) was manually threaded through a saline-filled, polyimide-fused silica capillary (Part #1,068,150,381; Polymicro Technologies Inc., Phoenix, AZ, USA). The capillary was sealed with clear epoxy at the recording end such that 100–200 μm of the fiber was left exposed, and the other end of the fiber was sealed to a silver wire with silver epoxy and silver paint. The silver wire/carbon fiber junction was encapsulated with clear epoxy for stability.

FSCV acquisition hardware was custom-built within MR-compatible aluminum casing (UNC Electronics Facility, Chapel Hill, NC, USA), and data were collected and analyzed

with the High Definition Cyclic Voltammetry (HDCV) computer program (Bucher et al., 2013). The standard coaxial cables used to carry signal from the electrodes to the headstage were replaced with MR-compatible triaxial cables. Triaxial cables were chosen to prevent current leakage via a driven shield, as well as to compensate for the additional cable capacitance introduced by the length of the cables necessary to connect the headstage to the electrodes through the back of the MRI bore (approximately 2 m). Output digitization was smoothed by passing digital waveform signals through a 2 kHz low-pass analog filter before being applied to the electrode. Input signals were split via T adapter and collected as raw current at one input channel (for analysis) and passed through an analog 2 kHz low-pass filter prior to collection on a second input channel (for real-time signal viewing). Ferrites were placed on both input and output voltage coaxial and triaxial cables to further eliminate high-frequency noise (Fair-Rite Products Corp., Wallkill, NY, USA). A 4th order Bessel low-pass filter (2 kHz cutoff frequency) was digitally applied to input currents post-acquisition.

Waveforms were applied to the microelectrodes to selectively oxidize and/or reduce dopamine and/or oxygen (Fig. 1). The oxygen-sensing waveform is an 11 ms waveform that holds at 0 V, scans up to +0.8 V, down to −1.4 V, then back to 0 V (Venton et al., 2003; Walton et al., 2017; Zimmerman and Wightman, 1991). The dopamine-sensitive waveform is an 8.5 ms triangular waveform with a −0.4 V holding potential that scans to +1.3 V and back to −0.4 V (Robinson et al., 2003; Venton et al., 2003). Waveforms were applied at 5 or 10 Hz, voltages were scanned at 400 V/s, and data were sampled at 100 kHz. All voltages are versus Ag/AgCl. In both calibration and in vivo studies, the oxygen-sensitive waveform was used prior to the dopamine-sensitive waveform.

A "dummy cell" was fabricated to characterize noise within the MRI bore, which consisted of a 30 kΩ resistor and 0.33 nF capacitor connected in series on a circuit board, to mimic solution resistance and carbon fiber electrode double-layer capacitance, respectively. Dopamine stock solutions and oxygen calibration solutions were freshly prepared in room temperature phosphate-buffered saline (pH 7.4). Flow-injection analysis was used to collect the current amplitude responses to an analyte bolus of known concentration (Kristensen et al., 1986). Concentrations from 100 to 2000 nM were injected in random order, and each concentration was injected in triplicate. The within-bore MRI flow-injection datasets were acquired with the gradient disabled with low-pass filtering, enabled without low-pass filtering, and enabled with low-pass filtering. These datasets were acquired in random order to ensure that noise from the enabled gradient had no detrimental effect on electrode sensitivity. Flow injection analysis data from within the MRI bore were not used to calibrate electrodes, as the tubing length required to keep the magnetic 6-port injector a safe distance from the MR heavily diluted the bolus concentrations. Flow-through analysis was repeated inside a Faraday cage to obtain calibration factors for pre- and post-implantation electrodes. Only oxygen waveform calibration data where the oxygen waveform was applied first are included (i.e., those that used the dopamine waveform first were excluded).

2.2. Animal care

All animal protocols were approved by the Institutional Animal Care and Use Committee of the University of North Carolina at Chapel Hill (UNC) in accordance with the National Institutes of Health Guide for Care and Use of Laboratory Animals (eighth edition). Nine male Long-Evans rats (300–450 g, Charles River, Wilmington, MA, USA) were pair-housed prior to surgery at UNC animal facilities, given food and water ad libitum, and kept on a 12 h light/dark cycle. These experiments characterize and use a new instrumental multimodality and analysis methodology, respectively, so subject sex was irrelevant and kept at males only. Care was taken to reduce the number of animals used. Three animals were excluded: Two animals had prohibitively large imaging artifacts, likely from the connective leads plugged into the stimulating electrode pedestal in the slices of interest, and one animal's electrode stopped functioning before the experiment finished.

2.3. Surgery

Rats were deeply anaesthetized with 4% isoflurane, placed in a rodent stereotaxic frame (Kopf, Tujunga, CA, USA), and maintained at 2% isoflurane. Depth of anesthesia was confirmed via toe pinch and eye blink responses. Coordinates are relative to skull at bregma (Paxinos and Watson, 2007). Holes were drilled over the ventral striatum (1.3 mm A-P, 2.0 mm M-L, 6.8–7.8 mm D-V) for the carbon-fiber microelectrode and the ventral tegmental area (VTA; −5.2 mm A-P, +1.2 mm M-L, −8.2 to −9.2 mm D-V) for the bipolar, MR-compatible twisted tungsten stimulating electrode (PlasticsOne, VA, USA); to avoid the sagittal sinus, the stimulating electrode was implanted at a 4° angle. The stimulating electrode was untwisted enough to separate the tips by 1 mm (Fortin et al., 2015). The D-V coordinates of the stimulating and working electrodes were optimized to evoke maximal dopamine release. The dopamine-sensitive waveform was used during implantation, so oxygen responses to stimulation were unknown prior to fMRI scanning. An additional 3–4 burr holes were drilled for MR-compatible, brass skull screws. An Ag/AgCl reference electrode wire was placed in the contralateral hemisphere. Silicone adhesive was applied around the working electrode (i.e., carbon-fiber microelectrode) to prevent cortical tissue damage from the heat of curing dental cement (Kwik-Sil, World Precision Instruments, Sarasota, FL, USA). Skull screws, electrodes, and plastic shield were held in place using dental cement. Subjects were singly-housed for at least 4 days to recover before scanning.

2.4. Phantom MRI

All MRI data were acquired using a Bruker 9.4 T MRI. In vitro scans used a Bruker 72 mm volume coil. An FSCV electrode was embedded within an agarose phantom and scanned to examine whether the materials induced artifacts in RARE (rapid acquisition with relaxation enhancement; BW=312.5 kHz, TR=2000 ms, TE=40 ms, in-plane resolution= 100 µm, slice thickness=100 µm) or FLASH (fast low angle shot; BW=312.5 kHz, TR=50 ms, TE=3.52 ms, in-plane resolution= 100 µm, slice thickness=100 µm).

2.5. FSCV-fMRI in vivo

In vivo BOLD fMRI data were acquired using a homemade surface coil, and subjects were prepared as described previously (Decot et al., 2017; Albaugh et al., 2016). BOLD

fMRI was chosen over the more sensitive (Kim et al., 2013) cerebral blood volume (CBV) fMRI as it is more commonly used and expected to acquire data more analogous to oxygen FSCV (Lowry et al., 2010). Briefly, subjects were anesthetized and paralyzed by infusing a cocktail of dexmedetomidine and pancuronium bromide (0.05 mg/kg/hr and 0.5 mg/kg/hr respectively, intraperitoneal) to prevent motion artifacts, supplemented with low dose isoflurane (0.5%), and artificially ventilated via endotracheal intubation. Experiments did not begin until rectal temperature stabilized at 37 ± 0.5 °C, end-tidal CO_2 was 2.6–3.2%, and oxygen saturation was 95%. Physiology was monitored throughout the experiment and maintained within normal ranges. Five-slice echo planar imaging (EPI) data were acquired with BW=333.33 kHz, TR=1000 ms, TE=15 ms, 80×80 matrix, FOV=2.56 cm^2, slice thickness=1 mm. Stimulation electrode pedestals caused an imaging artifact if implanted too close to the skull surface; one slice was discarded prior to data analysis to minimize the impact of its distortion on data analysis. EPI slice acquisition and electrical stimulations were both controlled via HDCV software. To interleave fMRI and FSCV data acquisition, HDCV sent a 10 ms, high-to-low TTL pulse to trigger EPI per-slice acquisition 3 ms after each applied FSCV waveform.

Oxygen challenges were administered and repeated in triplicate, where 100% medical air was inhaled for 60 s, then 100% oxygen for 60 s, and finally 100% medical air for 180 s. Medical air was generated onsite from ambient air via compressed air filtration. For deep brain stimulations, biphasic square-wave stimulations were administered 180 s apart, at 60 Hz with current amplitudes of 300, 500, and 700 μA, a 2 ms pulse-width, and total duration of 2 s. Each stimulation amplitude was administered in triplicate and in random order with simultaneously acquired oxygen FSCV, followed by a repeated set of randomly ordered triplicate stimulations per amplitude with simultaneously acquired dopamine FSCV. Finally, a powerful stimulation was given to evoke large responses for principal component analysis (PCA) training sets needed for FSCV analysis (60 Hz, 900 μA, 4 ms pulse-width, 4 s duration). A high-resolution RARE scan was obtained at the end of each scan to verify each electrode location (BW=183.1 kHz, TR=2500 ms, TE=33 ms, in-plane resolution=100 μm, slice thickness=1 mm).

2.6. Data analysis

FSCV data were analyzed within the HDCV analysis software, which can be licensed to academic users through the University of North Carolina Electronics Facility (University of North Carolina at Chapel Hill, Chapel Hill, NC, USA). FSCV data were background subtracted and filtered with a 4th order, 2 kHz cutoff low-pass Bessel filter. FSCV background currents were taken prior to each gas challenge or stimulation event. Post-implantation calibration factors from flow-through analysis, normalized to the length of the exposed carbon fiber, were used to quantify oxygen and dopamine concentrations. To verify that all faradaic currents resulted from oxygen or dopamine, data sets were analyzed using PCA within the HDCV analysis software (Bucher et al., 2013). Training sets for PCA consisted of 4–8 different concentrations per analyte of interest, per electrode. FSCV signal-to-noise ratios (SNRs) were calculated by subtracting a 10 s baseline average prior to stimulation from the maximum peak oxidative (dopamine) or reductive (oxygen) current,

then dividing the difference by the standard deviation of the same 10 s baseline period. FSCV data were binned to 1 s increments for all fMRI time-course comparisons.

BOLD fMRI data were pre-processed and analyzed in Analysis of Functional NeuroImages (AFNI) software (National Institute of Mental Health, Bethesda, MD, USA). Prior to preprocessing, all fMRI data were zero-padded to ensure that the data had a consistent and sufficient matrix size to be used as inputs for the AFNI image registration software. T2 anatomical and EPI fMRI data were manually aligned to a template using ITK-Snap. The first 8 TRs were excluded to account for steady state, and the first 8 s of FSCV time-courses were discarded to match. Data were interpolated in order to follow AFNI pre-processing pipeline slice requirements. After pre-processing, data matrices were truncated to their original size. BOLD time-courses were extracted using a region of interest (ROI) mask unique to each subject, based on the location of the tip of the FSCV microelectrode (Supplemental Fig. 1).

Head motion and baseline drift were removed by linear regression prior to first-level statistical analyses and ROI time-course extractions. Subject-level correlation maps were calculated using BOLD fMRI and oxygen FSCV time-courses from oxygen challenge and electrical stimulation experiments. Fisher z-transformations were performed on subject-level oxygen challenge and electrical stimulation correlation maps for group statistics. A one-sample *t*-test was performed using linear regression to identify voxel clusters that fit with the intercept line representing the average, at $p<0.05$. Benjamini/Hochberg false discovery rate (FDR) correction was used to correct the voxel-level multiple comparison problem, with a $q<0.05$ threshold. Then, a group average correlation map was generated using the surviving clusters. Subsequently, the inverse Fisher's Z-transform was performed to restore Fisher Z to Pearson's R correlation coefficients.

Sliding correlation analysis was used to determine if oxygen FSCV and BOLD fMRI time-courses synchronized (i.e., most highly correlated at time shift = 0 s) or if the modalities were sensitive to different aspects of hemodynamic change. Correlations between simultaneously acquired FSCV-fMRI time-courses were calculated, then one time-course would shift ±20 s in 1 s increments. A new correlation value was calculated for each incremental shift.

A dopamine-inclusive HRF was derived to estimate BOLD responses using ground-truth dopamine amplitude results from specific stimuli (i.e., an "output function"). First, oxygen ROI time-courses were low-pass filtered with a 0.05 Hz cutoff to remove physiological noise prior to deriving kinetic parameters (oxygen challenge) and subject-level HRFs (electrical stimulation). The dopamine-inclusive HRF was then derived at the subject-level using the linear system: BOLD(t) = DA(t) * HRF + baseline + linear drift(t), where BOLD(t) is the BOLD time-course of averaged voxels from within a subject ROI (Supplemental Fig. 1) and DA(t) is the simultaneously acquired dopamine FSCV time-course. DC offset and linear drift were removed from BOLD time-courses during HRF deconvolution analysis (Supplemental Fig. 2). All subject-level dopamine-inclusive HRFs were averaged, and the resulting group-level HRF was smoothed with a 3rd order Savitzky Golay filter. To identify brain regions that encode evoked dopamine amplitudes, a regressor matrix was

built from the smoothed, dopamine-inclusive HRF convolved with subject-level dopamine event time-courses, and a second-order polynomial curve (for detrending). Bayesian Ridge regression was used to get a more robust estimation against random noise compared to an ordinary least squares estimation, due to the relatively small sample size used in this study. The regression matrix was used in a general linear model (GLM) with voxel-wise BOLD data for group-level statistical analysis. A one-way ANOVA was used to test the main effects of the maximum evoked dopamine amplitude on HRF-derived contrast maps, using a permutation method (5000 times iteration) with the maximum T method for multi-voxel, multiple-comparison correction.

The typical method of estimating BOLD response maps convolves a block stimulus (i.e., "input function") with an established, canonical HRF function. In order to compare our dopamine-inclusive HRF prediction to a traditional HRF prediction, the latter was estimated via the AFNI 3dDeconvolve script that incorporates the following default gamma function: $HRF(t) = int(g(t-s), s = 0..min(t,d))$, where $g(t) = t^q*exp(-t)/(q^q*exp(-q))$, where t = time and $q = 5$. This stimulus-derived HRF predictor was used as a regressor for subject-level GLMs to identify significantly activated voxels from individual response maps. This group-level analysis used a one-tailed t-test to test mean subject-level regression coefficient maps against zero, with a $q = 0.05$ FDR threshold.

2.7. Code availability

Standard AFNI codes were used for BOLD fMRI pre-processing and traditional functional activation map analysis (https://afni.nimh.nih.gov). MATLAB (The Mathworks, Inc., Natick, MA, USA) codes for the time shift analysis and hemodynamic response function convolution will be made available upon request. Python codes to obtain statistical response maps and correlation maps are available at https://github.com/waltonlr/FSCV-fMRI_analysis_stats. Datasets will be made available on OpenNeuro (https://openneuro.org, DOI 10.18112/openneuro.ds003832.v1.0.0).

2.8. Statistical information

Statistics were performed using GraphPad Prism 8 (GraphPad Software, San Diego, CA, USA), AFNI, and Python. Repeated-measures analysis of variance (RM-ANOVA) was used to compare in vitro SNRs between multiple electrodes, with gradient and filter status as the within-subject factor. Maximum evoked BOLD and dopamine RM-ANOVA analyses were performed using stimulation amplitude as the within-subject factor. Significant ANOVA interactions were subjected to Tukey's post-hoc multiple comparisons analysis. FSCV and fMRI values for in vivo SNR data and oxygen challenge kinetic parameters were compared using two-tailed, ratio-paired t-tests. A $p<0.05$ threshold was used to indicate statistical significance in all analyses, and all statistical clusters were limited to clusters >50 voxels to exclude potential false positives.

3. Results

3.1. fMRI and FSCV compatibility

A major step to achieve simultaneous FSCV-fMRI is ensuring that FSCV material components do not produce imaging artifacts. Traditional glass capillary microelectrodes, like those used for FSCV, produce minor artifacts (Shyu et al., 2004), but polyimide-fused silica further enhances MR-compatibility (Yang et al., 2013) and is also used with FSCV microelectrodes (Fig. 2A) (Clark et al., 2010). Both in agarose phantoms and in vivo, polyimide-fused silica electrodes showed minimal MR artifacts (Fig. 2A–C); however, modifications were necessary to maximize MR compatibility. Standard fabrication connects the carbon fiber directly to a connection pin via silver epoxy, which provides structural support within the headcap and makes the electrode suitable for chronic implantation (Clark et al., 2010). Unfortunately, commercially available pins contain trace amounts of nickel, a magnetic material with large susceptibility artifacts (Schenck, 1996). Here, we silver epoxied the carbon fiber directly onto silver wires. Following implantation, 1 cm of silver wire from both working and Ag/AgCl reference electrodes was left exposed above the headcap during recovery (Fig. 2D). To protect the free-standing wires, plastic shields were cemented to the headcaps (Fig. 2D). We performed flow-through analysis to assess whether these modifications affected sensitivity. In our hands, the calibration factors for oxygen and dopamine on the oxygen-sensitive waveform were –0.19 nA/μM/100 μm and 4.8 nA/μM/100 μm, respectively (Supplemental Fig. 3a). Both calibration factors fall between values reported for glass microelectrodes (normalized to 100 μm) (Venton et al., 2003). On the dopamine-sensitive waveform, dopamine sensitivity was 34 nA/μM/100 μm, in agreement with the literature (Clark et al., 2010) (Supplemental Fig. 3b). These data indicate that our modified polyimide-fused silica electrodes are MR compatible and can detect analytes of interest with high sensitivity.

FSCV is a differential technique that detects electrooxidation and reduction reactions on the scale of nA or less (Fig. 1), so electrical noise must be minimized to maximize FSCV sensitivity. First, we placed a dummy cell (vide supra) inside the MRI bore to quantify ambient electrical noise. Sub-nA noise was achieved using minimal grounding and braided cables with the gradients disabled, but a 4th order Bessel low-pass filter with a 2 kHz cut-off frequency was necessary to remove the high amplitude, 50 kHz power amplifier noise present with enabled gradients (Supplemental Fig. 4). To ensure that noise levels were low enough to detect physiologically relevant concentrations of analyte, we performed a flow-injection experiment using dopamine boluses. A flow-injection cell was inserted into the MRI bore on a 3D printed holder, which attached to the same mobile sled that holds animals during scans (Fig. 3A). With repeated boluses, there was a significant main effect of the recording environment on the SNR ($F_{(1.8, 5.3)}$=40.9, $p = 0.0007$, Fig. 3B). Boluses recorded with the gradient enabled and without low-pass filtering had significantly lower SNR (6.46±2.63) than those recorded with low-pass filtering (disabled with filter: 135.9 ± 13.9, enabled with filter: 89.5 ± 16.0; Tukey's post-hoc, $p = 0.003$ and $p = 0.03$, respectively; Fig. 3B). Our chosen filter did not distort bolus amplitudes or shapes (Fig. 3C–D), making it an effective method of removing the majority of electrical noise within the MRI bore.

3.2.   Simultaneous fMRI and FSCV

It is well-documented with other electrical recoding modalities (e.g., electrophysiology) that EPI-based fMRI produces intrusive, high-amplitude noise during encoding, which can be removed via principal component regression, algorithms, data acquisition interleaving, or deleting encoding portions outright (Logothetis et al., 2001; Dong et al., 2018; Jaime et al., 2018; Huttunen et al., 2008). FSCV detects electrochemically active analytes via periodic electrooxidation/reduction voltage sweeps (Fig. 1). As EPI-based fMRI also delivers RF and gradient pulses periodically, ideally FSCV waveforms could interleave with active RF and gradient pulsing. A dummy cell was placed inside the bore during fMRI acquisition to observe the encoding artifact, which was approximately 2 V_{P-P}, 55 ms, and repeated with each slice acquisition (Fig. 3E–F). Any temporal overlap between the waveform application and EPI encoding resulted in high amplitude interference (Fig. 3E). To interleave FSCV and EPI recordings, MRI protocols were set to wait for a TTL trigger per slice and all timings were coordinated within the FSCV data acquisition software. FSCV software sends a high TTL to the MRI when data acquisition begins and remains high for 3 ms after each waveform application, then it switches to a 10 ms low TTL that triggers EPI slice acquisition (Fig. 3F). EPI repetition time (TR), FSCV waveform application frequency, and FSCV waveform duration must balance to avoid overlapping waveforms and EPI encoding. For example, a 10-slice EPI scan with 1000 ms TR (i.e., 100 ms between EPI artifacts) evenly interleaves with FSCV waveforms applied at 10 Hz (i.e., 100 ms between waveforms) for 10:1 FSCV:fMRI temporal resolution acquisition. The same EPI scan parameters also evenly interleave with 5 Hz FSCV; however, FSCV application frequencies that are not multiples of the TR value divided by the number of slices (e.g., 3 Hz) or that are too fast to repeat during the non-artifact TR time (i.e., 45 ms) will disrupt slice acquisition timing or overlap with EPI encoding, respectively. Timing parameters for each modality should be chosen with care to ensure that signals interleave cleanly without sacrificing temporal resolution; however, it is recommended that FSCV waveforms be applied at   5 Hz to detect rapid neurotransmitter kinetics (Belle et al., 2013). By using TTL trigger-dependent interleaving, one or more FSCV scans can be collected per EPI slice without encoding gradient interference.

3.3.   In vivo oxygen challenge in the NAc

Previous FSCV studies have shown that pharmacologically manipulating neurotransmission affects oxygen dynamics, which are taken to represent hemodynamic changes (Venton et al., 2003; Walton et al., 2017; Zimmerman et al., 1992); however, the spatial specificity of FSCV limits the interpretation to highly localized microenvironments. Using an oxygen-sensitive waveform (Fig. 4A), we simultaneously acquired oxygen-related signals from FSCV and fMRI, in vivo, at sampling volumes of different magnitudes (Fig. 4B). We first administered a 100% oxygen breathing challenge (Fig. 4A) and compared evoked responses within subject-level ROIs at the electrode tip implanted in the NAc (Supplemental Fig. 1). Both fMRI and FSCV oxygen changes increased during hyperoxia and fell to baseline afterwards (Fig. 4C, $n = 6$ subjects). The 40 s delay before oxygen levels change corresponds to the transit time between the gas flow source and the ventilated subject. FSCV data, binned to match fMRI temporal resolution (TR = 1000 ms), had significantly higher SNR during hyperoxia (FSCV: 47.7 ± 13.8, fMRI: 4.4 ± 0.4; $t_{(17)}=8.24$, $p < 0.0001$, $n = 18$ events; Fig. 4D). The averaged event time-courses highly correlated ($r = 0.85$, p

< 0.0001, $n = 18$ events; Fig. 4E) in agreement with the literature (Lowry et al., 2010). Subject-level time-courses also correlated despite being heavily weighted toward fluctuating baseline values (r 0.40, p<0.0001, $n = 6$ subjects; Fig. 5). However, there were differences between the observed oxygen kinetics (Fig. 4F, $n = 18$ events). The FSCV response preceded the highest correlated BOLD responses by 5 ± 2 s, according to time shift analysis ($n = 18$ events; Fig. 4F). The clearance time from the maximum response to half-max was significantly longer in BOLD fMRI versus oxygen FSCV ($n = 6$ subjects, FSCV: 20.7 ± 3.0 s, fMRI: 33.7 ± 3.4 s; $t_{(5)} = 4.48$, $p = 0.007$; Fig. 4G), but there was no difference in half-max rise times. The data trended towards a longer fMRI versus FSCV full-width at half-max (FWHM; $n = 6$ subjects, $t_{(5)}=2.21$, $p = 0.08$; Fig. 4G), but did not reach statistical significance. Though FSCV and fMRI detect highly correlated changes during an oxygen inhalation challenge, the difference in clearance kinetics indicate that these data are complementary. As expected of a systemic, uniform increase in oxygen from an inhalation challenge, induced BOLD responses and FSCV oxygen highly correlated spatially across the brain (one sample t-test, $p = 0.05$ compared to other voxels, followed by group statistics with $n = 6$ subjects; Fig. 4H). This analysis demonstrates the feasibility of using local FSCV signals for correlation/regression analysis at a whole brain scale.

3.4. In vivo electrical VTA stimulation

BOLD fMRI and oxygen FSCV map stimulus-evoked responses in the brain on different scales (Buxton, 2013; Venton et al., 2003; Walton et al., 2017). To demonstrate how FSCV-fMRI can study specific stimulus-evoked responses, we electrically stimulated the VTA (Fig. 6A). Evoked responses had higher SNR with FSCV versus fMRI responses within the NAc ROI (FSCV: 17.4 ± 3.2, fMRI: 3.3 ± 0.6; $t_{(17)}=5.40$, $p < 0.0001$, $n = 18$ events; Fig. 6B). Stimulations evoked positive oxygen FSCV and BOLD fMRI changes, which are characteristic of electrical VTA stimulation (Venton et al., 2003) (Fig. 6C). The averaged time-courses highly correlated ($r = 0.83$, $p < 0.0001$, $n = 18$ events; Fig. 6D). FSCV time-courses lagged the maximally correlated fMRI time-courses by 0.8 ± 0.8 s, according to time shift analysis (Fig. 6E). While traditional block-design GLM analysis extracted broad areas of VTA-induced BOLD responses (group GLM analysis with $n = 6$ subjects, clusters >50 voxels, $q = 0.05$ threshold; Fig. 7), similar to those reported in the literature (Brocka et al., 2018; Decot et al., 2017; Ferenczi et al., 2016), the brain areas showing the highest oxygen FSCV time-course correlations were more tightly localized to clusters in ipsilateral NAc, claustrum, and insular cortex, bilateral prelimbic and cingulate cortices, and septum (one sample t-test cutoff at $p = 0.05$ versus other voxels, followed by group GLM analysis with $n = 6$ subjects, clusters >50 voxels; Fig. 6F). Some bilateral voxels were noted in both analyses, but this is not unexpected of unilateral VTA stimulations (Fox et al., 2016). While the non-specific electrical stimulations used in these experiments could be powerful enough to activate the wide range of brain regions that are identified via canonical HRF predictions (Fig. 7), FSCV oxygen measurements could be used to identify subsets of traditional GLM-identified voxels that most closely match the hemodynamic response of an ROI.

Next, we recorded and analyzed simultaneous dopamine and BOLD data using FSCV-fMRI. The dopamine-sensitive FSCV waveform recorded high SNR dopamine measurements

during fMRI (29.2 ± 7.1; Fig. 6G). Evoked dopamine release preceded the hemodynamic response, in agreement with the literature (Venton et al., 2003) (Fig. 6H), and fMRI responses were consistent (i.e., fMRI responses during dopamine FSCV resembled those obtained during oxygen FSCV in Fig. 6C). One-way RM-ANOVA revealed that the maximum evoked BOLD fMRI in the NAc did not significantly change with stimulation amplitude (Fig. 6I), but evoked dopamine release did ($F_{(1.3,22.3)}$=39.2, $p < 0.0001$; Tukey's post-hoc, 300 vs 500 and 700 μA, $p < 0.0001$; 500 vs 700 μA, $p = 0.0014$; Fig. 6J). Deconvolution analysis was performed for each simultaneously acquired pair of BOLD and dopamine time-courses to derive subject-specific HRFs (Supplemental Fig. 2). The average of all subject-specific HRFs has an initial rise peaking at 7 s, undershoot peaking at 22 s, and a second increase above baseline peaking at 34 s (Fig. 6K). Because graded stimulation increased maximum dopamine release but not BOLD amplitudes in the NAc, we used this unique FSCV-fMRI dataset to identify spatial locations where the BOLD response covaried with the released dopamine amplitude. Each dopamine time-course ($n = 18$ events) was convolved with our derived HRF to form a GLM, then used to estimate subject-level contrast maps. The main effect of peak dopamine amplitude on the BOLD response identified significant BOLD activations in the prefrontal cortex and septum, where dopamine neurons also project (Bjö and Dunnett, 2007), as having encoded dopamine amplitude dependence ($p < 0.05$; Fig. 6L). Building upon the traditional neuroimaging analysis pipeline, neurotransmitter data from FSCV can provide an additional ground-truth regressor for fMRI data that is crucial for understanding how local neurotransmission can impact brain network dynamics.

4. Discussion

FSCV is a minimally invasive electrochemical technique used to detect neurotransmitters such as dopamine at a carbon-fiber microelectrode, and fMRI is a noninvasive way of mapping hemodynamic changes across the entire brain. A platform capable of monitoring dopamine and fMRI simultaneously has been desirable because how dopamine affects brain-wide activity dynamics is poorly understood (Bruinsma et al., 2018) and advancing this knowledge could make a tremendous impact on understanding dopaminergic drug mechanisms (Bruinsma et al., 2018), human behaviors (Lohrenz et al., 2016), and how to improve deep-brain stimulation therapies (Price et al., 2020). Existing FSCV and fMRI studies have used these techniques separately (Brocka et al., 2018; Lohrenz et al., 2016; Chang et al., 2012; Hosford et al., 2019), but one study indicated that simultaneous recordings could be possible (Kimble et al., 2009). In this study, we develop and characterize simultaneous FSCV-fMRI for the first time, in vitro and in vivo, within a 9.4 T MRI. Highly resolved oxygen changes via FSCV and concurrent BOLD fMRI detected complementary information about hemodynamics across multiple spatial and temporal scales in response to electrical stimulation and oxygen inhalation challenges (i.e., with and without induced neuronal activity increases). Electrically stimulated dopamine release and simultaneous BOLD fMRI data were collected, and we propose a way to use dopamine time-course information to identify specific brain regions that encode dopamine amplitudes. This technique bridges a critical gap between neurotransmitter activity and neuroimaging data and can help isolate the effect of chemical signaling on brain-wide hemodynamics.

We took advantage of the oxygen-sensing capabilities of FSCV and fMRI to cross-validate evoked hemodynamic changes at multiple scales. The hemodynamic response lags increased neuronal activity by up to several seconds (Buxton, 2013), so it can be observed using conventional FSCV and fMRI sampling rates (10 and 1 Hz, respectively). The sampling volumes of FSCV and fMRI, however, differ by orders of magnitude (10^5 μm^3 and 10^8 μm^3 for a 100 μm FSCV microelectrode sensing volume and single fMRI voxel, respectively) (Walton et al., 2017). This work required voxel clusters of 36±3 per ROI to obtain detectable fMRI responses, which further increased the spatial mismatch. We observed strong correlations between FSCV and fMRI time-courses in the NAc following oxygen challenges (Fig. 4E), in agreement with the only known study to perform simultaneous amperometric tissue oxygen detection and BOLD fMRI (Lowry et al., 2010); however, FSCV oxygen cleared faster (Fig. 4F). Extended hyperoxia decreases venous deoxyhemoglobin percentages, slows cerebral blood flow (Bulte et al., 2007), and pushes excess dissolved oxygen into surrounding tissues (Lowry et al., 2010). BOLD fMRI is weighted towards deoxyhemoglobin in venous blood vessels (Buxton, 2013), and FSCV detects tissue oxygen (i.e., oxygen diffused from blood vessels), so these techniques are sensitive to different oxygen dynamics. Thus, slower blood flow extends oxygenated hemoglobin clearance time from vessels within the fMRI ROI relative to tissue oxygen clearance from the much smaller FSCV sampling volume. Despite FSCV's faster temporal resolution, the onset kinetics of electrically evoked FSCV oxygen responses slightly lagged those of fMRI (Fig. 6C,H), in agreement with literature that performed these measurements separately (Hosford et al., 2019). These data indicate that with respect to tissue oxygen, hemoglobin oxygenation changes more rapidly in response to evoked neuronal activity than oxygen inhalation. It is possible that processes downstream of stimulated neuronal activity may more stringently regulate oxygen delivery within highly localized environments. Combining FSCV with more advanced, vessel-resolution fMRI techniques (Yu et al., 2016), or using FSCV arrays with fMRI, could further connect the knowledge gap between hemodynamic responses observed at these two different spatial scales.

Our simultaneous FSCV-fMRI experiments were performed in the NAc because the striatum has the highest concentration of dopamine terminals, and dopamine is a known vasomodulatory neurotransmitter (Krimer et al., 1998; Choi et al., 2006). Though the oxygen-sensitive waveform can detect dopamine (Venton et al., 2003; Zimmerman and Wightman, 1991) (Supplemental Fig. 3a), we quantified dopamine release using data from the dopamine-sensitive waveform (Bucher and Wightman, 2015) (Fig. 6G). The dopamine oxidation potential was shifted anodically during the scan versus during implantation (Supplemental Fig. 5a–b), an indication of reference and/or recording electrode biofouling seen with chronically implanted glass carbon-fiber microelectrodes (Rodeberg et al., 2017). The shift was not related to the magnetic field or active gradients, as it did not occur in vitro (Fig. 3B) and did occur in Faraday cage recordings from a subject given the same surgery and recovery period (Supplemental Fig. 5c). Though post-implantation electrodes showed decreased sensitivity in our hands, others saw consistent longitudinal responses (Clark et al., 2010). The evoked dopamine concentrations may also be lower than expected of our stimulation amplitudes due to a combination of exact recording (Park et al., 2010) and stimulating (Garris et al., 1993) electrode placements, and to dopamine release attenuation

that occurs after multiple electrical stimulations (Garris et al., 1993). Strategies to mitigate chronic implantation sensitivity problems are being researched (Hashemi et al., 2011; Seaton et al., 2020), but our data indicate that reliable, high SNR analyte detection during fMRI can still be achieved days after electrode implantation.

The ability to observe dopamine dynamics and whole-brain imaging simultaneously would enormously benefit research into global brain circuitry changes from drug abuse, pain, or disorders implicated in dopamine dysfunction (Brocka et al., 2018; Mandeville et al., 2013; Lohrenz et al., 2016; Bruinsma et al., 2018). By measuring and quantifying evoked dopamine release, FSCV-fMRI can generate data-driven HRFs (Fig. 6K) and help identify brain regions sensitive to different dopamine release amplitudes (Fig. 6L). These data can be used to study effects of neuronal or pharmacological manipulations and tease apart the role of dopaminergic signaling on local and global hemodynamic responses in healthy and pathological brains (Mandeville et al., 2013; Bruinsma et al., 2018). Our study chose an electrical stimulation protocol for FSCV to induce reliable dopamine changes in the NAc (Venton et al., 2003); however, neurochemicals other than dopamine are released in the NAc following electrical or optogenetic VTA dopaminergic neuron stimulation (Stuber et al., 2010), so these results do not establish dopamine as the sole neurochemical source responsible for the observed oxygen changes. Future studies that selectively drive dopamine release with confounding factors eliminated (e.g., suppressing neuronal activity and/or unwanted neurotransmission) will further isolate the role of dopamine and its receptors (Brocka et al., 2018; Decot et al., 2017).

Though our electrical stimulations lack specificity, the analysis framework proposed herein should set the foundation for neurotransmitter-based HRF modeling in the future. Interestingly, our dopamine-modeled HRF has two notable peaks, different from the single-peak canonical HRF (Lu et al., 2006). The first peak is the initial rise, and an additional peak occurs after the first post-stimulus undershoot. This "second peak" is well documented in the oxygen FSCV literature using both VTA and median forebrain bundle stimulations (Venton et al., 2003; Zimmerman and Wightman, 1991; Zimmerman et al., 1992), supporting our approach towards deriving an HRF to describe the relationship between concurrently measured neurochemical release and BOLD fMRI. Literature attributes these oxygen increases to cerebral blood flow (Zimmerman et al., 1992), and that each peak is mediated differently; for example, an adenosine receptor antagonist decimated the second peak response but had no effect on the first (Venton et al., 2003). Interestingly, blocking dopamine synthesis had no effect on either oxygen peak (Zimmerman et al., 1992). More research is needed to isolate dopamine and dopamine receptors' influence over HRFs, such as investigating responses to graded optogenetic stimulations that will probe a range of evoked dopamine amplitudes with greater specificity than electrical stimulations.

Our method using a ground-truth output metric (i.e., quantified dopamine release amplitudes) lends additional neurochemical context to response map interpretations and can pull out relationships that traditional input models (e.g., stimulation paradigms) would miss. For instance, though a traditional stimulus paradigm model with GLM pulled wide-spread activation around ipsilateral NAc (Fig. 7) similar to literature (Brocka et al., 2018; Decot et al., 2017; Ferenczi et al., 2016), maps of dopamine amplitude as the main effect isolated

prefrontal cortex and septum (Fig. 6L). Acquiring data from additional subjects or using CBV fMRI (Decot et al., 2017; Albaugh et al., 2016), which is more sensitive and spatially specific compared to BOLD fMRI (Kim et al., 2013), could confirm these effects and possibly reveal additional voxels that encode dopamine release amplitude. Our method utilizing ground truth data to guide models is more effective than relying on assumptions that the evoked response would scale with the given stimulus inputs and can account for inter-subject response variability. Further, mathematical models that predict dopamine-influenced hemodynamic changes heavily favor post-synaptic effects as the assumed driver of the fMRI response (Mandeville et al., 2013), and though these models have close agreement with actual data, they are subject to potentially flawed parameter values (e.g., receptor dissociation constants (Marcellino et al., 2012)). Bruinsma et al. summarize how both pre- and post-synaptic effects must be explored to tease apart dopaminergic contributions to BOLD fMRI responses, and how this can be accomplished using FSCV, fMRI, optogenetics, and pharmacology (Bruinsma et al., 2018). The ability to identify locations where brain activity co-varies with quantitative neurotransmitter amplitudes could have far-reaching benefits for research studying local neurotransmission influence over brain hemodynamics and behavior.

Though FSCV has been a common method of detecting in vivo neurotransmitters for decades, an increasing number of optical detection alternatives exist that could also pair with fMRI (Ganesana et al., 2017; Albers et al., 2018; Liang et al., 2017; Chen et al., 2019). A dopamine-sensitive protein-based MRI contrast agent has been used with BOLD (Li and Jasanoff, 2020), and dopamine dynamics have been explored using near-infrared fluorescent sensors (Beyene et al., 2019) and genetically encoded fluorescent sensors (Patriarchi et al., 2018; Sun et al., 2018). These techniques require either infusion cannulae or optical fibers for contrast agent dispersal or fluorescence detection, respectively, which use fMRI-compatible materials. These alternative dopamine detection methods have high spatiotemporal resolution, even exceeding FSCV, making them exciting potential multimodality expansions. These methods show qualitative percent changes in signal, so quantitative FSCV measurements could provide useful cross-validation. FSCV-fMRI remains a strong multimodality for studying dopaminergic influence on neurovascular coupling, as it requires a single implantation surgery, no genetic modifications or injections, and is the only current method available to measure electroactive neurotransmitter activity and whole-brain hemodynamics simultaneously. Importantly, FSCV is the fastest-resolution technique to quantify neurotransmitter release in humans (Bucher and Wightman, 2015; Kishida et al., 2011; Lohrenz et al., 2016; Chang et al., 2012), which is crucial for detecting rapid neurotransmission events during behavior. Our results may not directly translate to clinical observations due to the effect of anesthesia on functional connectivity (Paasonen et al., 2018; Stenroos et al., 2018; van Alst et al., 2019) and vascular responsivity (Dinh et al., 2021; Gao et al., 2017), but recent pioneering studies have made preclinical awake fMRI feasible (Stenroos et al., 2018; Dinh et al., 2021; Desjardins et al., 2019). Expanding this multimodality to include other anesthesia protocols (or lack thereof), neurotransmitter sensors, animal models, or techniques is a realistic possibility that could home in on the role of neurotransmitters in the hemodynamic response at multiple spatiotemporal scales in both preclinical and clinical experiments.

Supplementary Material

Refer to Web version on PubMed Central for supplementary material.

Acknowledgements

Abbreviations:

FSCV	fast-scan cyclic voltammetry
HRF	hemodynamic response function
NAC	nucleus accumbens
HDCV	high definition cyclic voltammetry
VTA	ventral tegmental area
PCA	principal component analysis

References

Albaugh DL, et al. , 2016. Functional Magnetic Resonance Imaging of Electrical and Optogenetic Deep Brain Stimulation at the Rat Nucleus Accumbens. Sci. Rep. 6, 1–13. [PubMed: 28442746]

Albers F, Wachsmuth L, van Alst TM, Faber C, 2018. Multimodal functional neuroimaging by simultaneous BOLD fMRI and fiber-optic calcium recordings and optogenetic control. Mol. Imaging Biol. 20, 171–182. [PubMed: 29027094]

Belle AM, Owesson-White C, Herr NR, Carelli RM, Wightman RM, 2013. Controlled iontophoresis coupled with fast-scan cyclic voltammetry/electrophysiology in awake, freely moving animals. ACS Chem. Neurosci. 4, 761–771. [PubMed: 23480099]

Beyene AG, et al. , 2019. Imaging striatal dopamine release using a nongenetically encoded near infrared fluorescent catecholamine nanosensor. Sci. Adv. 5.

Bjö A, Dunnett SB, 2007. Dopamine neuron systems in the brain: an update. Trends Neurosci 30, 194–202. [PubMed: 17408759]

Brocka M, et al. , 2018. Contributions of dopaminergic and non-dopaminergic neurons to VTA-stimulation induced neurovascular responses in brain reward circuits. Neuroimage 177, 88–97. [PubMed: 29723641]

Bruinsma TJ, et al. , 2018. The relationship between dopamine neurotransmitter dynamics and the blood-oxygen-level-dependent (BOLD) signal: a review of pharmacological functional magnetic resonance imaging. Front. Neurosci. 12, 238. [PubMed: 29692706]

Bucher ES, et al. , 2013. Flexible software platform for fast-scan cyclic voltammetry data acquisition and analysis. Anal. Chem. 85, 10344–10353. [PubMed: 24083898]

Bucher ES, Wightman RM, 2015. Electrochemical analysis of neurotransmitters. Annu. Rev. Anal. Chem. 8, 239–261.

Bulte DP, Chiarelli PA, Wise RG, Jezzard P, 2007. Cerebral perfusion response to hyperoxia. J. Cereb. Blood Flow Metab. 27, 69–75. [PubMed: 16670698]

Buxton RB, 2013. The physics of functional magnetic resonance imaging (fMRI). Reports Prog. Phys. 76.

Chang SY, et al. , 2012. Wireless fast-scan cyclic voltammetry to monitor adenosine in patients with essential tremor during deep brain stimulation. Mayo Clin. Proc. 87, 760–765. [PubMed: 22809886]

Chen X, et al. , 2019. Mapping optogenetically-driven single-vessel fMRI with concurrent neuronal calcium recordings in the rat hippocampus. Nat. Commun. 10, 5239. [PubMed: 31748553]

Choi J–K, Chen YI, Hamel E, Jenkins BG, 2006. Brain hemodynamic changes mediated by dopamine receptors: role of the cerebral microvasculature in dopamine-mediated neurovascular coupling. Neuroimage 30, 700–712. [PubMed: 16459104]

Clark JJ, et al. , 2010. Chronic microsensors for longitudinal, subsecond dopamine detection in behaving animals. Nat. Methods 7, 126–129. [PubMed: 20037591]

Decot HK, et al. , 2017. Coordination of brain-wide activity dynamics by dopaminergic neurons. Neuropsychopharmacology 42, 615–627. [PubMed: 27515791]

Desjardins M, et al. , 2019. Awake mouse imaging: from two-photon microscopy to blood oxygen level–dependent functional magnetic resonance imaging. Biol. Psychiatry Cogn. Neurosci. Neuroimaging 4, 533–542. [PubMed: 30691968]

Dinh TNA, Jung WB, Shim HJ, Kim SG, 2021. Characteristics of fMRI responses to visual stimulation in anesthetized vs. awake mice. Neuroimage 226, 117542. [PubMed: 33186719]

Dong L, et al. , 2018. Neuroscience information toolbox: an open source toolbox for EEG–fMRI multimodal fusion analysis. Front. Neuroinform. 12, 56. [PubMed: 30197593]

Ferenczi EA, et al. , 2016. Prefrontal cortical regulation of brainwide circuit dynamics and reward-related behavior. Science 351. [PubMed: 27463660]

Fortin SM, Cone JJ, Ng-Evans S, McCutcheon JE, Roitman MF, 2015. Sampling phasic dopamine signaling with fast-scan cyclic voltammetry in awake, behaving rats. Curr. Protoc. Neurosci. 2015 7.25.1–7.25.20. [PubMed: 25559005]

Fox ME, et al. , 2016. Cross-hemispheric dopamine projections have functional significance. Proc. Natl. Acad. Sci. U. S. A. 113, 6985–6990. [PubMed: 27298371]

Ganesana M, Lee ST, Wang Y, Venton BJ, 2017. Analytical techniques in neuroscience: recent advances in imaging, separation, and electrochemical methods. Anal. Chem. 89, 314–341. [PubMed: 28105819]

Gao YR, et al. , 2017. Time to wake up: studying neurovascular coupling and brain-wide circuit function in the un-anesthetized animal. Neuroimage 153, 382–398. [PubMed: 27908788]

Garris PA, Collins LB, Jones SR, Wightman RM, 1993. Evoked extracellular dopamine in vivo in the medial prefrontal cortex. J. Neurochem. 61, 637–647. [PubMed: 8336146]

Hashemi P, et al. , 2011. Chronically implanted, nafion-coated Ag/AgCl reference electrodes for neurochemical applications. ACS Chem. Neurosci 2, 658–666. [PubMed: 22125666]

Hosford PS, et al. , 2019. Electrochemical carbon fiber-based technique for simultaneous recordings of brain tissue PO2, pH, and extracellular field potentials. Biosens. Bioelectron. X 3.

Huttunen JK, Gröhn O, Penttonen M, 2008. Coupling between simultaneously recorded BOLD response and neuronal activity in the rat somatosensory cortex. Neuroimage 39, 775–785. [PubMed: 17964186]

Iadecola C, 2017. The Neurovascular Unit Coming of Age: a Journey through Neurovascular Coupling in Health and Disease. Neuron 96, 17–42. [PubMed: 28957666]

Jaime S, Cavazos JE, Yang Y, Lu H, 2018. Longitudinal observations using simultaneous fMRI, multiple channel electrophysiology recording, and chemical microion-tophoresis in the rat brain. J. Neurosci. Methods 306, 68–76. [PubMed: 29778509]

Kim S–G, et al. , 2013. Cerebral blood volume MRI with intravascular superparamagnetic iron oxide nanoparticles. NMR Biomed 26, 949–962. [PubMed: 23208650]

Kimble CJ, et al., 2009. Wireless instantaneous neurotransmitter concentration sensing system (WINCS) for intraoperative neurochemical monitoring. In: Proceedings of the 31st Annual International Conference of the IEEE Engineering in Medicine and Biology Society: Engineering the Future of Biomedicine, EMBC 2009. IEEE Computer Society, pp. 4856–4859 vol. 2009.

Kishida KT, et al. , 2011. Sub-second dopamine detection in human striatum. PLoS ONE 6.

Krimer LS, Christopher Muly E, Williams GV, Goldman-Rakic PS, 1998. Dopaminergic regulation of cerebral cortical microcirculation. Nat. Neurosci. 1, 286–289. [PubMed: 10195161]

Kristensen EW, Wilson RL, Wightman RM, 1986. Dispersion in Flow Injection Analysis Measured with Microvoltammetric Electrodes. Anal. Chem. 58, 986–988.

Li N, Jasanoff A, 2020. Local and global consequences of reward-evoked striatal dopamine release. Nature 580, 239–244. [PubMed: 32269346]

Liang Z, Ma Y, Watson GDR, Zhang N, 2017. Simultaneous GCaMP6-based fiber photometry and fMRI in rats. J. Neurosci. Methods 289, 31–38. [PubMed: 28687521]

Logothetis NK, Pauls J, Augath M, Trinath T, Oeltermann A, 2001. Neurophysiological investigation of the basis of the fMRI signal. Nature 412, 150–157. [PubMed: 11449264]

Lohrenz T, Kishida KT, Montague PR, 2016. BOLD and its connection to dopamine release in human striatum: a cross-cohort comparison. Philos. Trans. R. Soc. B Biol. Sci. 371, 20150352.

Lowry JP, et al. , 2010. Real-time electrochemical monitoring of brain tissue oxygen: a surrogate for functional magnetic resonance imaging in rodents. Neuroimage 52, 549–555. [PubMed: 20417284]

Lu Y, et al. , 2006. Using voxel-specific hemodynamic response function in EEG-fMRI data analysis. Neuroimage 32, 238–247. [PubMed: 16774839]

Mandeville JB, et al. , 2013. A receptor-based model for dopamine-induced fMRI signal. Neuroimage 75, 46–57. [PubMed: 23466936]

Marcellino D, Kehr J, Agnati LF, Fuxe K, 2012. Increased affinity of dopamine for D2-like versus D1-like receptors. Relevance for volume transmission in interpreting PET findings. Synapse 66, 196–203. [PubMed: 22034017]

Meyer-Lindenberg A, et al. , 2002. Reduced prefrontal activity predicts exaggerated striatal dopaminergic function in schizophrenia. Nat. Neurosci. 5, 267–271. [PubMed: 11865311]

Miyazaki I, Asanuma M, Diaz-Corrales FJ, Miyoshi K, Ogawa N, 2004. Direct evidence for expression of dopamine receptors in astrocytes from basal ganglia. Brain Res 1029, 120–123. [PubMed: 15533323]

Oh Y, et al. , 2018. Tracking tonic dopamine levels in vivo using multiple cyclic square wave voltammetry. Biosens. Bioelectron. 121, 174–182. [PubMed: 30218925]

Paasonen J, et al. , 2017. Dose-response effect of acute phencyclidine on functional connectivity and dopamine levels, and their association with schizophrenia-like symptom classes in rat. Neuropsychopharmacology 119, 15–25.

Paasonen J, Stenroos P, Salo RA, Kiviniemi V, Gröhn O, 2018. Functional connectivity under six anesthesia protocols and the awake condition in rat brain. Neuroimage 172, 9–20. [PubMed: 29414498]

Park J, Aragona BJ, Kile BM, Carelli RM, Wightman RM, 2010. In vivo voltammetric monitoring of catecholamine release in subterritories of the nucleus accumbens shell. Neuroscience 169, 132–142. [PubMed: 20451589]

Patriarchi T, et al. , 2018. Ultrafast neuronal imaging of dopamine dynamics with designed genetically encoded sensors. Science 360.

Paxinos G, Watson C, 2007. The Rat Brain in Stereotaxic Coordinates. Elsevier.

Price JB, et al. , 2020. Clinical applications of neurochemical and electrophysiological measurements for closed-loop neurostimulation. Neurosurg. Focus 49, E6.

Ren J, Xu H, Choi J–K, Jenkins BG, Chen YI, 2009. Dopaminergic response to graded dopamine concentration elicited by four amphetamine doses. Synapse 63, 764–772. [PubMed: 19484725]

Robinson DL, Venton BJ, Heien MLAV, Wightman RM, 2003. Detecting subsecond dopamine release with fast-scan cyclic voltammetry in vivo. Clin. Chem. 49, 1763–1773. [PubMed: 14500617]

Rodeberg NT, Sandberg SG, Johnson JA, Phillips PEM, Wightman RM, 2017. Hitchhiker's guide to voltammetry: acute and chronic electrodes for in vivo fast-scan cyclic voltammetry. ACS Chem. Neurosci. 8, 221–234. [PubMed: 28127962]

Schenck JF, 1996. The role of magnetic susceptibility in magnetic resonance imaging: MRI magnetic compatibility of the first and second kinds. Med. Phys. 23, 815–850. [PubMed: 8798169]

Seaton BT, Hill DF, Cowen SL, Heien ML, 2020. Mitigating the effects of electrode biofouling-induced impedance for improved long-term electrochemical measurements in vivo. Anal. Chem. 92, 6334–6340. [PubMed: 32298105]

Shyu B–C, Lin C–Y, Sun J–J, Sylantyev S, Chang C, 2004. A method for direct thalamic stimulation in fMRI studies using a glass-coated carbon fiber electrode. J. Neurosci. Methods 137, 123–131. [PubMed: 15196834]

Stenroos P, et al. , 2018. Awake rat brain functional magnetic resonance imaging using standard radio frequency coils and a 3D printed restraint kit. Front. Neurosci. 12, 548. [PubMed: 30177870]

Stuber GD, Hnasko TS, Britt JP, Edwards RH, Bonci A, 2010. Dopaminergic terminals in the nucleus accumbens but not the dorsal striatum corelease glutamate. J. Neurosci. 30, 8229–8233. [PubMed: 20554874]

Sun F, et al. , 2018. A genetically encoded fluorescent sensor enables rapid and specific detection of dopamine in flies, fish, and mice. Cell 174, 481–496. [PubMed: 30007419]

Thompson JK, Peterson MR, Freeman RD, 2003. Single-neuron activity and tissue oxygenation in the cerebral cortex. Science 299, 1070–1072. [PubMed: 12586942]

van Alst TM, et al. , 2019. Anesthesia differentially modulates neuronal and vascular contributions to the BOLD signal. Neuroimage 195, 89–103. [PubMed: 30930308]

Venton BJ, Michael DJ, Wightman RM, 2003. Correlation of local changes in extracellular oxygen and pH that accompany dopaminergic terminal activity in the rat caudate-putamen. J. Neurochem. 84, 373–381. [PubMed: 12558999]

Walton LR, Boustead NG, Carroll S, Wightman RM, 2017. Effects of glutamate receptor activation on local oxygen changes. ACS Chem. Neurosci. 8, 1598–1608. [PubMed: 28425701]

Yang P–F, et al. , 2013. Comparison of fMRI BOLD response patterns by electrical stimulation of the ventroposterior complex and medial thalamus of the rat. PLoS ONE 8.

Yu X, et al. , 2016. Sensory and optogenetically driven single-vessel fMRI. Nat. Methods 13, 337–340. [PubMed: 26855362]

Yung KKL, et al. , 1995. Immunocytochemical localization of D1 and D2 dopamine receptors in the basal ganglia of the rat: light and electron microscopy. Neuroscience 65, 709–730. [PubMed: 7609871]

Zimmerman JB, Kennedy RT, Wightman RM, 1992. Evoked neuronal activity accompanied by transmitter release increases oxygen concentration in rat striatum in vivo but not in vitro. J. Cereb. Blood Flow Metab. 12, 629. [PubMed: 1618942]

Zimmerman JB, Wightman RM, 1991. Simultaneous electrochemical measurements of oxygen and dopamine in vivo. Anal. Chem. 63, 24–28. [PubMed: 1810167]
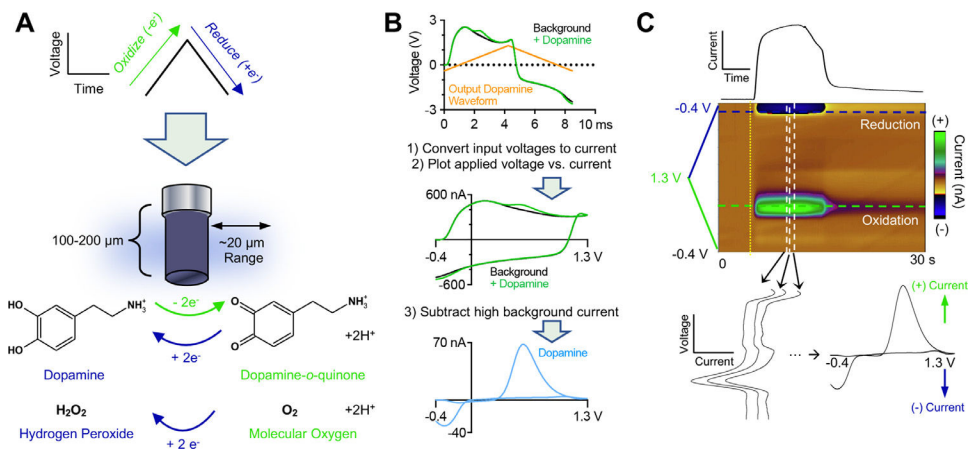
Fig. 1.

FSCV detects electrochemically active analytes. (A) Voltage sweeps (waveforms) are applied to a carbon-fiber microelectrode at a specified frequency and scan rate to electrochemically oxidize and/or reduce chemical analytes (i.e., subtract and/or add electrons [e-], respectively). (B) High voltage scan rates produce large but stable background currents that can be subtracted to obtain analyte cyclic voltammograms. *Top*: Dopamine waveform time-course compared to voltages recorded at the carbon-fiber microelectrode with (green) and without (black) dopamine present. *Middle:* Recorded voltages are first converted to current via hardware gain settings, then plotted versus applied voltage. *Bottom:* Background currents are subtracted to obtain analyte cyclic voltammograms and visually indicate the chemical(s) detected at the carbon-fiber microelectrode surface. (C) FSCV data are displayed as 3D color plots. *Top*: Horizontal slices from color plots give time-courses; for maximum sensitivity, time-courses from its oxidation potential are used for dopamine quantification (green dashed line). *Middle*: Color plot of a dopamine bolus, where time is on the x-axis, applied voltage is on the y-axis, and current amplitudes are indicated in false color. *Bottom*: Background current from a time-point without the analyte of interest present (yellow dotted line) is subtracted from vertical slices on the color plot (white dashed lines) to give background-subtracted current versus voltage plots. These are then plotted as cyclic voltammograms.
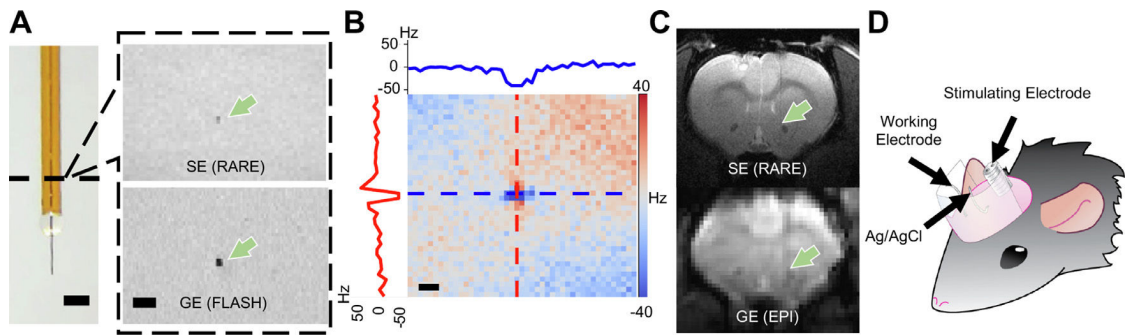
Fig. 2.
Modifying FSCV materials improves MRI compatibility. (A) *Left*: Polyimide-fused silica capillary microelectrode (scale bar=100 μm). *Right*: Electrode axial cross-section scanned inside an agarose phantom using spin echo (SE) rapid acquisition with relaxation enhancement (RARE), and gradient echo (GE) fast low angle shot (FLASH) sequences (scale bar=1 mm). (B) Axial view of the magnetic field map showing inhomogeneities induced by the microelectrode materials in an agar phantom. Scale bar=200 μm. Frequency profiles are taken from the dashed line cross-section of the same color (horizontal=blue, vertical=red). (C) Microelectrodes implanted in the rat NAc in vivo, indicated with arrows, during a SE-based RARE anatomical scan and a GE-based echo planar imaging (EPI) functional scan. (D) Rat headcaps were fitted with plastic shields to protect loose silver wire connections to FSCV working and reference electrodes.
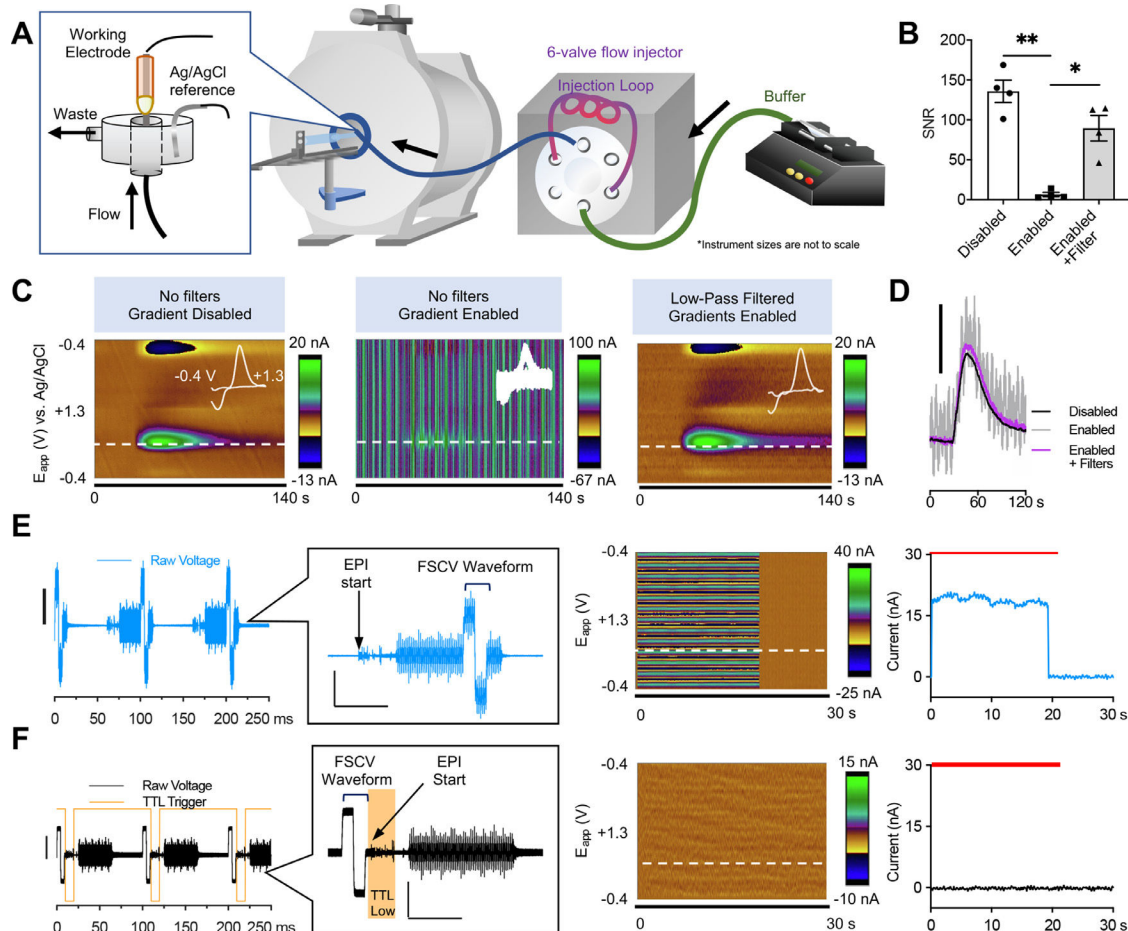
Fig. 3.

Software and hardware modifications for simultaneous FSCV-fMRI. (A) Within-bore flow-injection analysis requires the 6-port injection valve to be placed outside of the magnet at a safe distance. A fresh dopamine bolus is injected and flowed through to the electrode inside of the MRI bore for detection. (B) SNR for a physiologically relevant dopamine concentration. Averaged triplicate measures are shown ($n = 4$ electrodes; Tukey's post-hoc $*p < 0.05$, $**p < 0.01$). (C) Low-pass digital Bessel filters remove the high-frequency noise from enabled MRI gradients without distorting FSCV signals. Color plots indicate flow-injection dopamine boluses within the MRI bore. Cyclic voltammograms obtained from the maximum bolus current are overlaid in white. (D) Dopamine bolus injection time-courses from the dopamine oxidation potential in C. Scale bar=15 nA. (E,F) Dummy cell data collected inside the MRI bore during EPI scanning. *Left*: Time-courses of raw input voltage from the FSCV headstage acquired at 100 kHz (triangular applied waveforms appear square due to charging current at the electrode; see Fig. 1B). Scale bar=4 V (magnification inset: vertical scale bar=1 V, horizontal scale bar=20 ms). Orange box indicates the low TTL duration that triggers EPI acquisition. *Middle*: 3D color plot of low-pass filtered data. White dashed line indicates the dopamine oxidation potential. *Right*: Current time-course at the dopamine oxidation potential from the corresponding color plot. Red bar indicates EPI scan
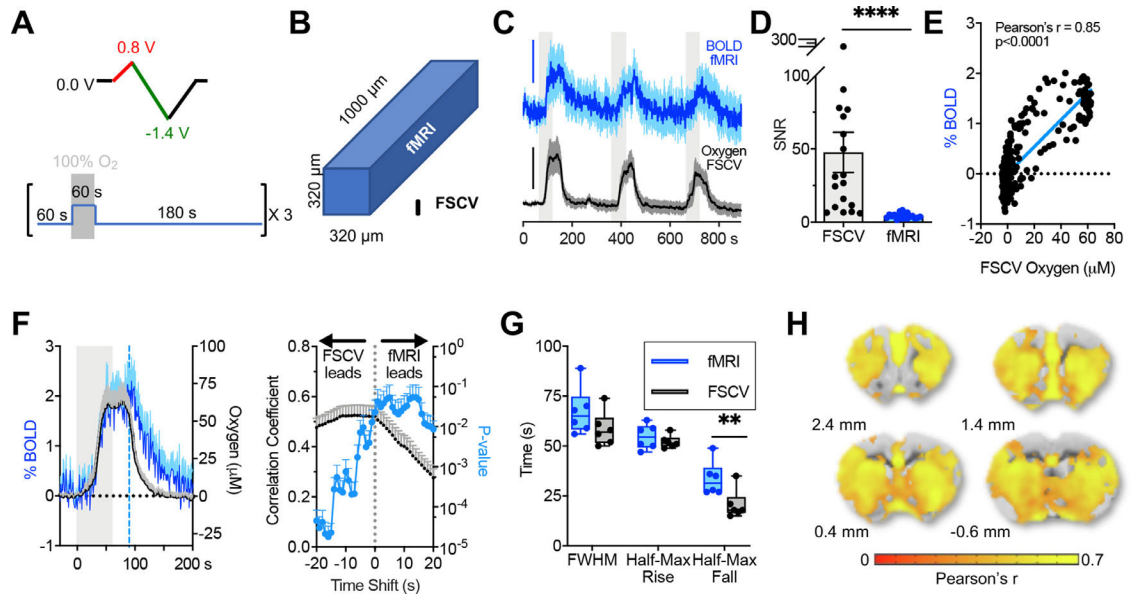
duration. Large artifacts appear when FSCV waveforms and EPI encoding times overlap temporally (E), but interleaving the signals with TTL triggers avoids this interference (F).

Fig. 4.

BOLD fMRI and oxygen FSCV time-courses in the rat NAc highly correlate during oxygen breathing challenges. (A) Paradigm schematic. *Top*: An oxygen-sensitive waveform was repeated throughout the recording session to detect oxygen changes. Red indicates the oxidation potential sweep, green indicates the reduction potential sweep. *Bottom:* Oxygen inhalation event paradigm. When not inspiring pure oxygen, subjects inspired medical air. (B) A single BOLD fMRI voxel compared to the volume sampled by FSCV, to scale. (C) BOLD fMRI and oxygen FSCV time-courses show signal increases during oxygen inhalation periods ($n = 6$ subjects). Blue scale bar=2% signal change. Black scale bar=50 μM oxygen. (D) SNR from FSCV and fMRI NAc ROI oxygen inhalation time-courses ($n = 18$ events, ROIs=36±3 voxels). (E) Averaged BOLD fMRI and oxygen FSCV time-course correlation ($n = 18$ events). (F) Averaged oxygen challenge event time-courses from C (*left*) were analyzed using sliding correlations (*right*). Correlations were calculated for every 1 s iteration that the BOLD fMRI time-course was stepped forward or backward relative to actual acquisition time (i.e., time shift = 0 s). (G) Kinetic parameters derived from subject-averaged time-courses, where half-max rise is the time from $t = 0$ to half-max, and half-max fall is the time from $t = 30$ s after the 100% oxygen ends (indicated in f as a blue dashed line) to the half-max clearance value ($n = 6$ subjects). (H) Group-level correlation between BOLD fMRI and concurrently acquired oxygen FSCV time-courses ($p = 0.05$). Voxels with correlation coefficient <0.3 are excluded. gray boxes in A, C, and F indicate times where gas inhalation lines were switched to 100% oxygen. Error bars are ±SEM or +SEM, for visual clarity. Ratio-paired *t*-test **$p < 0.01$, ****$p < 0.001$.
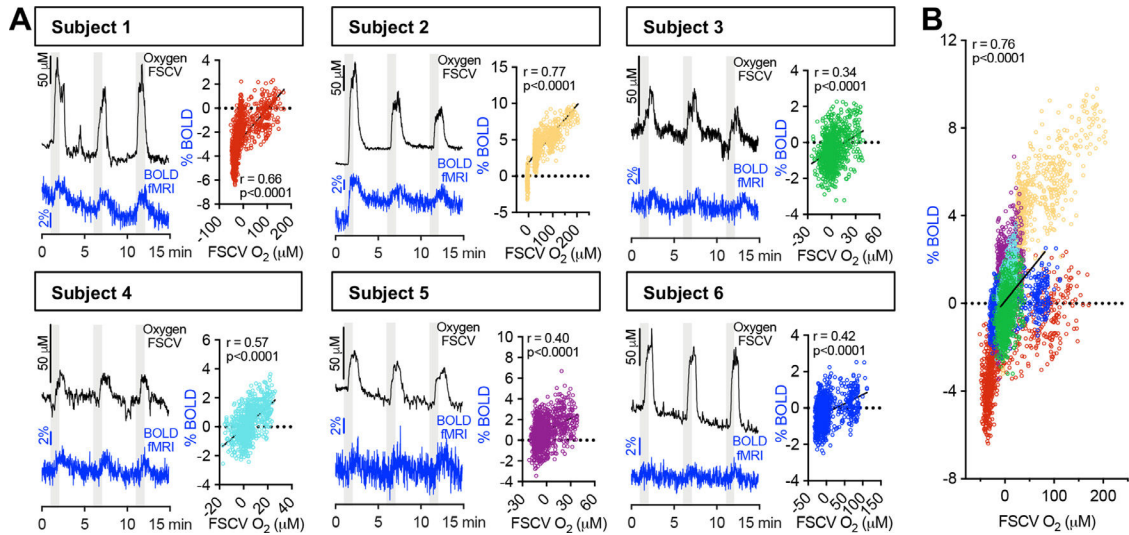
Fig. 5.
Subject-level correlations between BOLD fMRI and FSCV oxygen changes detected during repeated 100% oxygen inhalation challenges. (A) Each subject subpanel consists of a single FSCV oxygen time-course (black) and the simultaneously acquired BOLD fMRI time-course (blue) averaged from all voxels within its electrode-focused ROI (Supplementary Fig. 1) to the left, and a correlation plot for the full 15 min oxygen inhalation session data points to the right. gray boxes indicate the 60 s epochs where subjects' air supply was 100% oxygen. (B) Correlation of all individual oxygen inhalation challenge data points, where colors correspond to subjects' colors in (A).
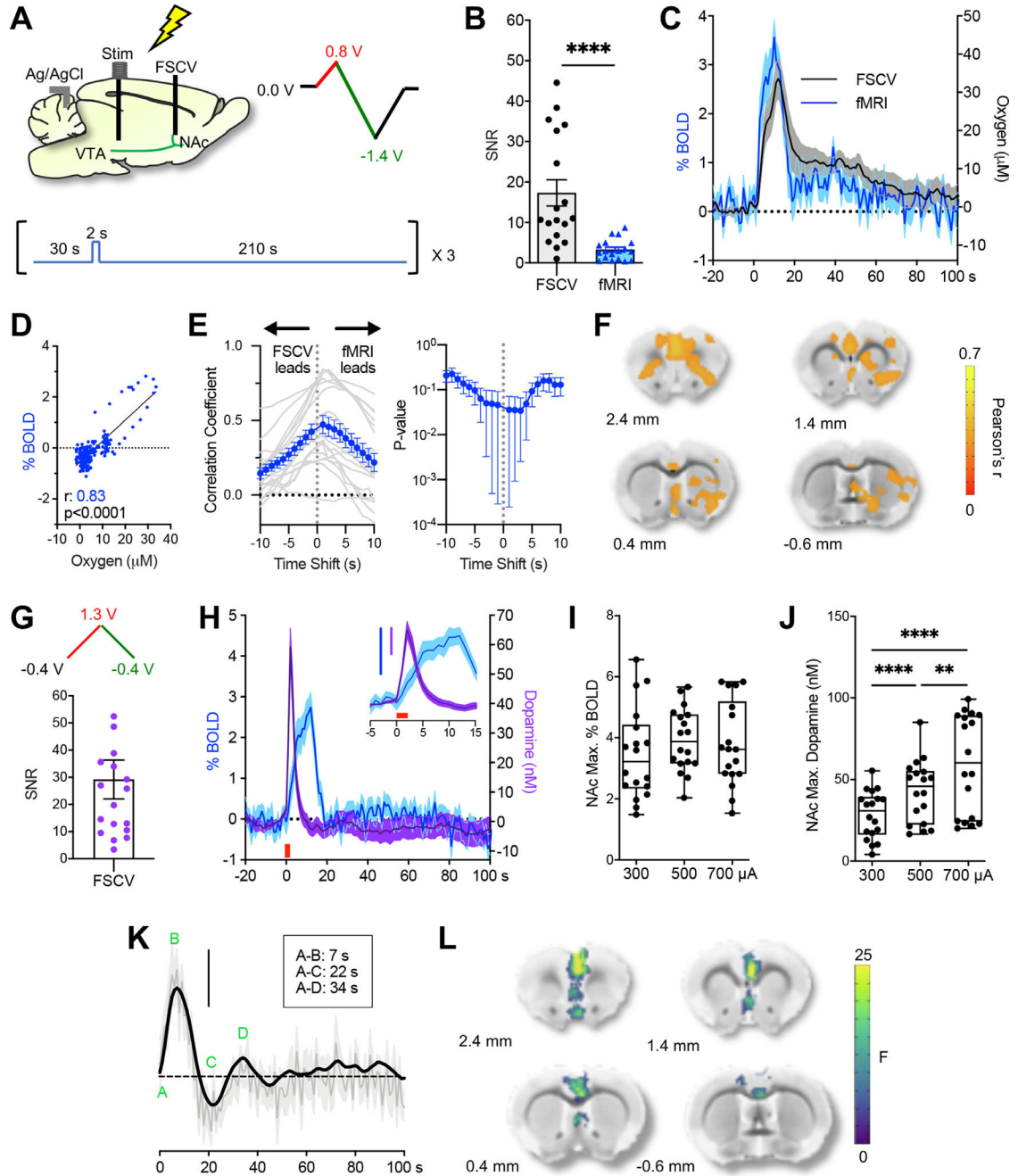
Fig. 6.

Simultaneous FSCV-fMRI recordings during electrical VTA deep-brain stimulation, using both tissue oxygen FSCV and dopamine FSCV waveforms (2 s, 700 μA, 60 Hz, 2 ms pulse width). (A) Paradigm schematic for electrical stimulations. *Top:* Cartoon of implant locations (*left*), and the oxygen-sensitive FSCV waveform used (*right*). Red indicates the oxidation potential sweep, green indicates the reduction potential sweep. *Bottom:* Electrical stimulation paradigm. (B) SNR values from FSCV and fMRI ROIs during individual stimulation time-courses (*n* = 18 events, ROIs=36±3 voxels; ratio-paired *t*-test ****p* < 0.001). (C) Time-courses from NAc recording sites during ipsilateral electrical

VTA stimulation ($n = 18$ events). (D) Pearson's correlation of averaged BOLD fMRI and FSCV oxygen time-courses from c. (E) BOLD fMRI and oxygen FSCV sliding time shift correlations. The average of all event-level correlation coefficients (*left*) and p-values (*right*) between BOLD fMRI and oxygen FSCV for a given time shift are indicated in blue ($n = 18$ events). Individual event-level correlation coefficients are indicated in gray as a connective line for visual clarity. (F) Group-level correlation maps between FSCV oxygen and BOLD fMRI time-courses ($p = 0.05$). Voxels with correlation coefficients <0.3 are excluded. (G) Dopamine-sensitive FSCV waveform used for the second set of electrical stimulations (*top*), and the SNR for FSCV dopamine (*bottom; n = 18* events). (H) Time-courses from NAc recording sites during the second set of ipsilateral electrical VTA stimulations. Stimulation duration is indicated with a red bar. Inset is a magnification; blue scale bar=2% BOLD response, purple scale bar=20 nM dopamine. (I) Maximum evoked NAc BOLD fMRI values and (J) FSCV dopamine release from different amplitude stimuli (one-way RM-ANOVA, Tukey's post-hoc $**p < 0.01$, $****p<0.001$). (K) Group-level dopamine-derived HRF. Averaged HRF is gray, with smoothed HRF overlaid in black. Scale bar=2% of BOLD response, and the dashed line represents the BOLD baseline. (L) GLM model maps derived from voxel-wise BOLD fMRI using the dopamine-inclusive HRF convolved with subject-level dopamine time-courses as a regressor, along with a second-order polynomial for detrending. Contrast indicates voxels that have a significant main effect with evoked dopamine amplitude (one-way ANOVA, $p < 0.05$ significance threshold for clusters >50 voxels). Error bars are ±SEM.
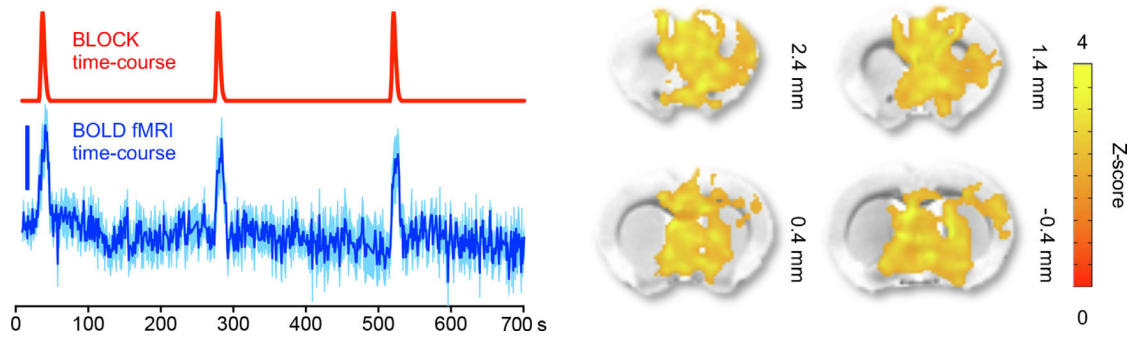
Fig. 7.
Electrical VTA deep-brain stimulation data from Fig. 6H analyzed using a stimulus paradigm-based fMRI analysis. A block design paradigm based on the stimulation duration (*left*; 2 s stimulations) was convolved with a canonical HRF for GLM analysis (*right*, one-sided *t*-test with $q = 0.05$ threshold, $n = 6$ subjects). Error bars are ±SEM. Scale bar for BOLD fMRI time-course=2% signal change.